RSC Advances

ROYAL SOCIETY OF CHEMISTRY

www.rsc.org/advances

$Ni_{0.33}Mn_{0.33}Co_{0.33}Fe_2O_4$ nanoparticles anchored on oxidized carbon nanotubes as advanced anode materials in Li-ion batteries

Zailei Zhang,*[a] Guangwei Kan,[a] Wenfeng Ren,[a] Qiangqiang Tan,*[a] Ziyi Zhong[b] and Fabing Su*[a]

[a]*State Key Laboratory of Multiphase Complex Systems, Institute of Process Engineering, Chinese Academy of Sciences, Beijing, China 100190,*

[b]*Institute of Chemical Engineering and Sciences, A*star, 1 Pesek Road, Jurong Island, Singapore 627833*

* To whom correspondence should be addressed. E-mail address: zhangzl@ipe.ac.cn (Z. Zhang); qtan@ipe.ac.cn (Q. Tan); fbsu@ipe.ac.cn (F. Su), Tel.: +86-10-82544850, Fax: +86-10-82544851.

Abstract

We report a solvothermal synthesis of $Ni_{0.33}Mn_{0.33}Co_{0.33}Fe_2O_4$ (NMCFO) nanoparticles anchored on the surface of oxidized carbon nanotubes (OCNT) to form NMCFO/OCNT nanocomposites as advanced anode materials in Li-ion batteries. $Ni(CH_3COO)_2$, $Mn(CH_3COO)_2$, $Co(CH_3COO)_2$, and $FeCl_3$ were employed as the metal precursors and CH_3COONa, $HOCH_2CH_2OH$ and H_2O as the mixed solvent in the synthesis. The obtained samples were characterized by X-ray diffraction, thermogravimetric analysis, inductively coupled plasma optical emission spectrometry, X-ray photoelectron spectroscopy, transmission electron microscopy, and scanning electron microscopy. It is found that the OCNT provided functional groups on the outer walls to nucleate and anchor NMCFO nanoparticles (5−20 nm), while retaining the inner walls intact with high conductivity. Compared with the bare NMCFO nanoparticles, NMCFO/OCNT composites showed a significantly improved electrochemical performance because OCNT can substantially inhibit the aggregation of NMCFO nanoparticles and buffer the volume change, and moreover, the inner walls of OCNT provide excellent electronic conduction pathways. This work opens an effective way for the fabrication of ferrite-based metal oxide/OCNT hybrid as promising anode materials for Li-ion batteries.

Keywords: nickel manganese cobalt ferrite, oxidized carbon nanotubes, electrochemical performance, Li-ion batteries

1. Introduction

To achieve higher specific capacities than that of the conventional graphite (372 mAh g^{-1}), in recent years nanosized metal oxides such as NiO,[1] Fe_2O_3,[2] Co_3O_4,[3,4] $ZnMn_2O_4$,[5] $CoMn_2O_4$,[6] and $MnFe_2O_4$[7] have been intensively studied as anode materials in Li-ion batteries (LIBs). However, severe aggregation of the particles and volume change of the electrode materials during discharge/charge processes often lead to poor cycling stability, sluggish kinetics in charge transfer and ionic diffusion, as well as high intrinsic resistance.[8-11] These shortcomings can induce additional performance degradation of the metal oxide based electrodes, especially at high current densities, seriously limiting their practical application.[12] To circumvent the above technical barriers, conductive carbon materials are often incorporated with metal oxides to form metal oxides/carbon composites, such as Fe_2O_3@carbon,[13] Fe_3O_4 nanoparticles embedded in porous carbon,[14] Co_3O_4 coated on carbon nanotube,[15] mesoporous carbon-encapsulated NiO,[16] CoO coated on graphene,[17] carbon nanofibers@$CoMn_2O_4$ coaxial nanocables,[18] and mesoporous $Mn_{0.5}Co_{0.5}Fe_2O_4$ nanospheres grown on grapheme,[19] which have partially improved the cycling stability and rate capability.[20, 21] These nanostructured metal-oxide-containing electrodes with small size are able to partially buffer the stress and strain effects caused by the particle volume expansion/contraction during the Li-ion insertion/extraction, thus improving the cycling and rate capability.[22] Meanwhile, the instructive guidelines for designing high-performance nanostructured hybrid materials based on metal oxides and carbon for LIBs have been established via these research activities.[23]

Iron-based oxides have recently received increased attention as very promising anode materials for rechargeable LIBs because of their high theoretical capacity, non-toxicity, low cost, and improved safety.[24] Meanwhile, nanostructured carbon nanotubes (CNT) are also promising anode materials for LIBs due to their large electrode/electrolyte contact area and active surface, high chemical stability and conductivity, and good mechanical strength.[25-31] Therefore, in the past decade efforts were made to synthesize CNT-metal oxides nanoparticle hybrids or composites.[32, 33] The binding between CNT and

metal oxides nanoparticles are quite diverse, e.g., by noncovalent interactions (such as π–π stacking and hydrophobic wrapping), electrostatic interactions, or by covalent bonding through functionalization of outer wall by oxidation.[34-36] Xu et al. prepared NiO/CNT composites as anode material using nitric acid treated CNT, which maintained the capacity at ~800 mAh g^{-1} after 50 discharge/charge cycles at a current density of 50 mA g^{-1}.[37] Zhuo et al. prepared Co_3O_4/CNT composites using oxidative treatment on CNT, which left a large number of acidic groups on the surface, showing 776 mAh g^{-1} at the 100th cycle at a current density of 200 mA g^{-1}.[15] In addition, Wang et al. found that the carbon coated a-Fe_2O_3 hollow nanohorns supported on nitric acid treated CNT backbones exhibited a very stable capacity retention of 800 mAh g^{-1} over 100 cycles at a current density of 500 mA g^{-1}.[12] From these literature results, it is found that metal oxides/CNT hybrids, in which the CNT are pre-oxidized partially, exhibit good electrochemical performance by virtue of their advantageous structural features. However, so far there has no report showing attractive hybrid containing multicomponent ferrite-based metal oxides nanoparticles and CNT for lithium storage.

Herein, we report a novel synthsis of $Ni_{0.33}Mn_{0.33}Co_{0.33}Fe_2O_4$ (NMCFO)/oxidized carbon nanotubes (OCNT) composites by directly growing NMCFO nanoparticles on OCNT. In this strategy, NMCFO nanoparticles are uniformly dispersed on the surface of OCNT to form NMCFO/OCNT network nanocomposites. Compared with the bare NMCFO nanoparticles, NMCFO/OCNT exhibits significantly improved electrochemical performance with excellent cycling stability and high rate performance, suggesting a potential application as anodes in future LIBs with a high energy density.

2. Experimental

2.1 Material synthesis

2.1.1 Synthesis of oxidized carbon nanotubes (OCNT)

All the chemicals were of analytical grade and purchased from Sinopharm Chemical Reagent Co., Ltd. The OCNT were made by a modified Hummers method.[38] Carbon nanotubes (CNT) (CNano

Technology (Beijing) Ltd.) were first purified by calcination at 500 °C for 2 h and washed with diluted HCl (10 %). The purified CNT (2 g) were put into a 250 mL round-bottom flask, followed with addition of 50 ml of concentrated sulfuric acid, and the mixture was stirred at room temperature overnight. Next, the flask was heated in an oil bath at 40 °C, and 0.5 g of $NaNO_3$ was added and dissolved in the suspension. This step was followed with a slow addition of 2.0 g of $KMnO_4$, and the reaction temperature was maintained at 40 °C. The solution was stirred for 30 min. Afterward, 100 mL of water was slowly added to the flask. After 30 min, the flask was removed from the oil bath, followed with addition of 300 mL of water and 30 mL of 30 % H_2O_2 to terminate the reaction. After stirred at room temperature for 15 min, the sample was then repeatedly centrifuged and washed with 10 % HCl solution for several times, rinsed with copious amounts of water. The final precipitate was dispersed in 20 mL of water and lyophilized. Finally, a dry product of ~1.9 g was collected.

2.1.2 Synthesis of $Ni_{0.33}Mn_{0.33}Co_{0.33}Fe_2O_4$/oxidized carbon nanotubes (NMCFO/OCNT)

All the chemicals were of analytical grade and purchased from Sinopharm Chemical Reagent Co., Ltd. In a typical synthesis, $Ni(CH_3COO)_2 \cdot 4H_2O$ (0.33mmol), $Mn(CH_3COO)_2 \cdot 4H_2O$ (0.33mmol), $Co(CH_3COO)_2 \cdot 4H_2O$ (0.33mmol), $FeCl_3 \cdot 6H_2O$ (2.0 mmol), $CH_3COONa \cdot 3H_2O$ (10.0mmol) and OCNT(x g) were dissolved/dispersed in distilled water (40 mL) and $HOCH_2CH_2OH$(40 mL) to form a homogeneous slurry, which was then refluxed for 2 h at 110 °C under constant stirring in a three-neck flask. Subsequently, the mixture was sealed in a stainless-steel autoclave and heated at 200 ℃ for 48 h. The resulting precipitates were collected by centrifugation, washed with distilled water and absolute ethanol, and finally dried in vacuum at 120 ℃ for 24 h. The obtained NMCFO/OCNT nanocomposites containing OCNT (x g) 0.20, 0.15, 0.10, and 0.05 g of OCNT were denoted NMCFO/OCNT-1, NMCFO/OCNT-2, NMCFO/OCNT-3, and NMCFO/OCNT-4, respectively. Similarly, bare NMCFO was prepared without adding OCNT, and NMCFO/CNT prepared by adding un-oxidized 0.10 g CNT. In addition, amorphous NMCFO/OCNT precursor was prepared as a comparison as follows: $Ni(CH_3COO)_2 \cdot 4H_2O$ (0.33mmol), $Mn(CH_3COO)_2 \cdot 4H_2O$ (0.33mmol), $Co(CH_3COO)_2 \cdot 4H_2O$

(0.33mmol), $FeCl_3$ $6H_2O$ (2.0 mmol), CH_3COONa $3H_2O$ (10.0mmol) and OCNT (0.10 g) were dissolved/dispersed in distilled water (40 mL) and $HOCH_2CH_2OH$ (40 mL) to form a homogeneous slurry, which was then refluxed for 2 h at 110 °C under constant stirring in a three-neck flask. The resulting precipitates were collected by centrifugation, washed with distilled water and absolute ethanol, and finally dried in vacuum at 120 ℃ for 24 h to obtain the amorphous NMCFO/OCNT precursors.

2.2 Materials characterization

X-ray diffraction patterns (XRD) were recorded on a PAN analytical X'Pert PRO MPD using the Cu Kα radiation of (λ = 1.5418 Å). The microscopic feature of the samples was characterized by field-emission scanning electron microscopy (FESEM) with an energy-dispersive X-ray spectrometer(EDX) (JSM-7001F, JEOL, Tokyo, Japan) and transmission electron microscopy (TEM) with an energy-dispersive X-ray spectrometer(EDX) (JEM-2010F, JEOL, Tokyo, Japan) operated at 300V. Thermogravimetric (TG) analysis was carried out on an EXSTAR TG/DTA 6300 (Seiko Instruments, Japan) at a heating rate of 10 ℃ min^{-1} in air (200 mL min^{-1}). The elemental analysis was conducted by inductively coupled plasma optical emission spectrometry (ICP-OES, Optima 5300DV,Pekin Elmer, US). X-ray photoelectron spectroscopy (XPS) analysis was carried out on an ESCALab250electron spectrometer from Thermo Scientific Corporation using monochromatic 150W Al Ka radiation. Pass energy for then arrow scan was 30 eV. The chamber pressure was about 6.5×10^{-10} mbar. The binding energies were referenced to the C1s line at 284.8 eV.

2.3 Electrochemical measurement

The working electrode was prepared by mixing the active materials, acetylene black, and polyvinylidene fluoride (PVDF) in a weight ratio of 80:10:10 with N-methylpyrrolidone (NMP) as a solvent. The resulting slurries were cast onto a common Cu foil (current collector). The film composed of Cu foil and slurries were rolled into 25 μm thin sheets, and then dried at 50 °C for 24 h. The film were cut into disks with a diameter of 14 mm, and then dried at 120 ^oC in vacuum for 24 h. CR2016

coin-type cells were assembled in an Ar-filled glove box with lithium foils as the counter electrodes and polypropylene microporous films (Celgard 2400) as separators. The liquid electrolyte is 1 mol L^{-1} $LiPF_6$ in a mixture of ethylene carbonate (EC) and dimethyl carbonate (DMC) (1:1, v/v). The galvanostatic charge and discharge tests were carried out on a NEWARE CT-3008-5V10mA testing instrument in a voltage range between 0.01 and 3.0 V at current densities of 50, 100, 500, and 1000 mA g^{-1}. Cyclic voltammetry (CV) was carried out using a CHI660D potentiostat in the voltage range of 0–3 V at a scanning rate of 0.1 mV s^{-1} at room temperature. Electrochemical impedance spectroscopy (EIS) measurements were also conducted using the CHI660D potentiost at over a frequency range from 100 kHz to 10 mHz with an ac oscillation of 5 mV.

3. Results and discussion

The carbon nanotubes (CNT) used in this work are about 12 nm in diameter and several micrometers in length.[39] A modified Hummers method[38] was used to prepare OCNT under mild oxidation. As determined by X-ray photoelectron spectroscopy (XPS), the OCNT contains ~15 at. % oxygen (Fig. S1). Fig. 1a shows the XRD patterns of all the samples. The observation of the strong (002) peak at 2θ values of about 26.3° in OCNT indicates its high graphite crystallinity (JCPDS No. 25-0284). The observed diffraction peaks at 2θ values of 30.1, 35.6, 43.4, 53.7, 57.3, and 62.8° correspond to the lattice planes of (220), (311), (400), (422), (511), and (440) respectively, indicating the formation of crystal $Ni_{0.33}Mn_{0.33}Co_{0.33}Fe_2O_4$ (NMCFO) in the samples of NMCFO, NMCFO/OCNT-1, NMCFO/OCNT-2, NMCFO/OCNT-3, and NMCFO/OCNT-4.[40]

Fig. 1b shows the TG curves of all the samples. The impurity of CNT is around 4.2 wt%, probably due to the presence of metal catalyst (Fe/Co/Ni) residue after the synthesis of CNT. However, these metal nanoparticles have been removed by calcination followed with washing by dilute hydrochloric acid for OCNT. It can be seen that the weight loss derived from carbon combustion is located between

360–600 ^{o}C for OCNT, lower than that for CNT (400–650 ^{o}C), indicating the lowered combustion temperature of OCNT after the oxidation treatment. For the bare NMCFO nanoparticles, the weight loss of about 1.2 wt% may be derived from the trace amount of organic residue on their surface. For NMCFO/OCNT composites, the weight loss starts at about 230 ^{o}C, lowering than that of OCNT (360 ^{o}C). This is because the presence of metal oxides (NMCFO) can catalytically promote the carbon combustion process at a lower temperature.[41] The measured weight loss of NMCFO/OCNT-1, NMCFO/OCNT-2, NMCFO/OCNT-3, and NMCFO/OCNT-4 is about 41.7, 36.2, 28.9, and 16.7 wt% respectively in the temperature range from 100 to 1000 °C, which can be ascribed to the decomposition of organic species and the combustion of OCNT, suggesting that the weight percentage of OCNT is approximately at 40.5, 35.0, 27.7, and 15.5 wt% in the samples of NMCFO/OCNT-1, NMCFO/OCNT-2, NMCFO/OCNT-3, and NMCFO/OCNT-4, respectively.

Fig. 2a shows the TEM image of NMCFO nanoparticles with a size range of 5–20 nm. Most of the NMCFO nanoparticles are agglomerated together due to the surface effect of nanoparticles.[42] Meanwhile, the HRTEM image of these nanoparticles (Fig. 2b) reveals that the lattice fringe spacing is about 0.293 nm, corresponding to the interplanar distance of (220) planes in NMCFO,[40] and each nanoparticle is actually a single crystal. The EDX spectrum of NMCFO nanoparticles in Fig. 2c demonstrates the presence of Ni, Mn, Co, Fe, and O elements. The elemental mapping images based on the NMCFO nanoparticles show the homogeneous distribution of all the five elements (Ni, Mn, Co, Fe, and O) (Fig. S2). The atomic ratio of Ni, Mn, Co, and Fe elements is approximate 1: 1 : 1 : 6 from ICP-OES analysis. In fact, it is possible to tune the atomic ratio of $Ni_xMn_yCo_zFe_2O_4$ ($x+y+z=1$, $0<x, y, z<1$) by controlling the ratio of raw materials ($Ni(CH_3COO)_2$, $Mn(CH_3COO)_2$, and $Co(CH_3COO)_2$). For example, for $Ni_{0.2}Mn_{0.4}Co_{0.4}Fe_2O_4$, the used raw materials amount is 0.2 mmol $Ni(CH_3COO)_2$, 0.4 mmol $Mn(CH_3COO)_2$, and 0.4 mmol $Co(CH_3COO)_2$ (Fig. S3a); while for $Ni_{0.4}Mn_{0.4}Co_{0.2}Fe_2O_4$, the corresponding amount is 0.4 mmol $Ni(CH_3COO)_2$, 0.4 mmol $Mn(CH_3COO)_2$, and 0.2 mmol $Co(CH_3COO)_2$ (Fig. S3b). The SEM image in Fig. 2d shows that the formed NMCFO/OCNT

precursors have network structure. NMCFO and OCNT in NMCFO/OCNT precursors can be easily differentiated by the brightness contrast in the TEM images (Fig. S4b and S4c), which shows that the NMCFO are amorphous and coated on the surface of OCNT, well agreement with the XRD result (Fig. S4a). Also, it is very important to identify the amorphous nature of NMCFO precursors, as it helps to understand the formation process of the crystallized NMCFO.

The SEM image of Fig. 3a shows that the OCNT are coated with NMCFO nanoparticles forming the network structure after adding 0.20 g OCNT in NMCFO/OCNT-1. The surface of the OCNT becomes coarser after coating with the smaller NMCFO nanoparticles. When the OCNT amount is decreased to 0.15 (Fig. 3b) and 0.10 g (Fig. 3c and 3d), most of NMCFO nanoparticles are coated on the surface of OCNT forming the NMCFO/OCNT-2 and NMCFO/OCNT-3 network composites. With further decrease of the OCNT amount to 0.05 g (Fig. S5a), larger portion of NMCFO nanoparticles is aggregated together but still coated on the surface of OCNT. Therefore, it is possible to tune the nanocomposites network structure and composition by varying the synthesis conditions such as the amount of OCNT and raw chemicals, as well as the reaction time and temperature.

More detailed structural information can be obtained from the TEM results. The TEM images of NMCFO/OCNT-1 in Fig. 4a and 4b show that smaller NMCFO nanoparticles are highly dispersed on the surface of OCNT after adding 0.20 g OCNT. Fig. 4c shows the high resolution TEM image of NMCFO/OCNT-1, in which, the NMCFO nanoparticles with a size of around 15 nm are attached to the surface of OCNT and the lattice with an interplanar spacing of about 0.293 nm corresponds to the (220) plane of NMCFO, consistent with the observation in Fig. 2b. The HRTEM image also reveals that the inner walls of graphitic carbon nanotubes in the hybrid are still well maintained or not broken (Fig. 4c), suggesting that the inner walls of OCNT were not destroyed by the oxidation treatment and the subsequent reactions during the hybrid synthesis. After addition of 0.15 g and 0.10 g OCNT, the samples of NMCFO/OCNT-2 (Fig. 4d and 4e) and NMCFO/OCNT-3 (Fig. 4f and 4g) with uniformly coated NMCFO nanoparticles on the surface of OCNT composites are obtained. However, with further

decrease of the OCNT amount to 0.05 g, most of NMCFO nanoparticles and OCNT are aggregated together (Fig. S5b and S5c). The crystal NMCFO and OCNT in NMCFO/OCNT composites also could be easily differentiated by the brightness contrast in the TEM images (Fig. 4, Fig. S5b and S5c). These crystal NMCFO nanoparticles are attached to the surface of OCNT to form network composites, consistent with the above SEM observation.

The formation process of NMCFO/OCNT composites is illustrated in Fig. 5. Firstly, Ni^{2+}, Mn^{2+}, Co^{2+}, and Fe^{3+} dissolved in the solvent are adsorbed on the external surface of the OCNT, because OCNT with functional groups on the outer walls is a good metal ion adsorbent (Fig. 5a).[15, 38] With the increase of the temperature to 110 ℃, these metal ions are accumulated specifically on the outer wall by the oxidative functional groups on OCNT.[35] These oxidative functional groups can act as heterogeneous nucleation sites in the early reaction stage to facilitate the formation of small amorphous nanoparticles during the precipitation.[43] Thereafter, the small amorphous NMCFO nanoparticles are generated and aggregated on the surface of OCNT via the reaction ($0.33Ni^{2+} + 0.33Mn^{2+} + 0.33Co^{2+} + 2Fe^{3+} + 4H_2O \rightarrow Ni_{0.33}Mn_{0.33}Co_{0.33}Fe_2O_4 + 8H^+$) with the water generated from the metal precursors (Fig. 5b). With the further increase of the temperature to 200 ℃, the amorphous NMCFO nanoparticles are crystalized to form crystal NMCFO nanoparticles (Fig. 5c), which are also coated on the surface of the OCNT. And in the last stage, the crystal NMCFO/OCNT network composites are developed and formed (Fig. 5d). In case with addition of more OCNT, it will have more oxidative functional groups acting as the adsorption sites for the given amounts of Ni^{2+}, Mn^{2+}, Co^{2+}, and Fe^{3+}. As a result, the formed NMCFO will become smaller in size and be dispersed more uniformly on the OCNT surface as shown in Fig. 3, Fig. 4, and Fig. S5. This is because of the dispersing effect of OCNT. In a control experiment, it was failed to get the uniform distribution of NMCFO nanoparticles and CNT network composites by using 0.10 g CNT without oxidization. Therefore, it is clear that the oxidative functional groups on the external surface of OCNT are the nucleation centers and play the key role in the growth of NMCFO nanoparticles.

Fig. 6a presents the CV curves of NMCFO/OCNT-1 in the first two cycles, and in the 51th cycle after 50 rate discharge-charge cycles at a scan rate of 0.1 mV s^{-1}. In the first scan, two cathodic peaks are observed at about 0.57 and 0.78 V, which correspond to the conversion reactions of Fe^{3+}, Co^{2+}, Ni^{2+}, and Mn^{2+} to their metallic states and the formation of Li_2O, respectively. The broad anodic peak from 1.0 V to 2.0 V can be ascribed to the oxidation reactions of metallic Fe, Co, Ni, and Mn. The quaternary metal oxide NMCFO stores Li through reversible formation and decomposition of Li_2O. In the second scan, the reduction peaks are shifted to 0.73 and 1.51 V respectively. The peak intensity and integral areas of the 51th cycle after 50 rate discharge-charge cycles measurement are almost the same as those of the second cycle for NMCFO/OCNT-1, which demonstrates the good reversible oxidation-reduction reaction, and reversible formation and decomposition of Li_2O.[44] The discharge and charge capacities in the first run, and their initial coulombic efficiencies are shown in Fig. S6 and Table 1. The discharge-charge capacity for NMCFO component may be based on the oxidation-reduction of metallic Fe, Co, Ni, and Mn nanoparticles to $Ni_{0.33}Mn_{0.33}Co_{0.33}Fe_2O_4$ respectively via the reaction: $4Li_2O + 0.33Ni + 0.33Mn + 0.33Co + 2Fe \leftrightarrow Ni_{0.33}Mn_{0.33}Co_{0.33}Fe_2O_4 + 8Li^+ + 8e^-$. A distinct voltage plateau can be clearly identified at ca. 0.8–0.9 V, which is corresponding to the reduction of Fe^{3+} to Fe, Co^{2+} to Co, Ni^{2+} to Ni, and Mn^{2+} to Mn during the initial discharge process (Fig. S6). Meanwhile, a clear plateau is observed in the charge process at ca. 1.5–2.5 V, which is corresponding to the oxidation of Fe to Fe^{3+}, Co to Co^{2+}, Ni to Ni^{2+}, and Mn to Mn^{2+} during the initial charge process (Fig. S6). The carbon lithiation and delithiation voltage plateau are not observed, because of the small contribution of carbon to the overall anode capacity in term of the previous reports (Fig. S6).[39]

The cycling performance in Fig. 6b and Table 1 shows that the discharge capacity of NMCFO/OCNT-1, NMCFO/OCNT-2, NMCFO/OCNT-3, NMCFO/OCNT-4 after 100 cycles is around 673.7, 733.1, 710.3, and 506.3 mAh g^{-1}, respectively, which is higher than that of NMCFO (141.8 mAh g^{-1}) and OCNT (296.4 mAh g^{-1}) (Fig. S7). It should be mentioned that the capacity of NMCFO/OCNT composites after 100 cycles is lower than that of the CoNiO nanowire arrays loaded

on TiO_2 nanotubes (1097 mAh g^{-1} after 40 cycles at a current density of about 606 mA g^{-1}),[45] and carbon-coated graphene/Fe_3O_4 nanosheets (920 mAh g^{-1} after 100 cycles at a current density of 200 mA g^{-1}).[46] As reported in ref (40), the discharge capacity after 60 cycles was about 487.2 mAh g^{-1} for NMCFO mesoporous nanospheres, which is higher than that of the NMCFO nanoparticles (141.8 mAh g^{-1} after 100 cycles). Probably the porosity structure of NMCFO nanospheres could buffer the large volume change of anodes caused by the conversion reaction during the repeated Li^+ insertion/extraction,[47] and be an advantage for lithium-storage applications that require rapid ion transport and large contact area between the electrode and the electrolyte. In addition, the more added acetylene black in ref (40) could inhibit the aggregation of NMCFO nanospheres, and provide effective electronic conduction pathways. After 200 cycles, the discharge capacity of NMCFO/OCNT-1 at the current densities of 50 and 500 mA g^{-1} still maintains at about 624.8, and 421.0 mAh g^{-1}, as shown in Fig. S8, indicating the good cycling performance of the composite anode. The average coulombic efficiency after the second cycle and average capacity fading rate during the 100 cycles of all above NMCFO/OCNT samples is shown in Table 1. Clearly, in a certain range, the more the OCNT added, the better the electrochemical performances will be for the formed network structure composites.

Fig. 6c showed the charge/discharge profiles of NMCFO/OCNT-1 of the first cycles at different current densities. NMCFO/OCNT-1 has a better rate performance than NMCFO/OCNT-1 as shown in Fig. 6d and Fig. S9. In favor of the presence of conductive OCNT, these network composite materials exhibit much lower resistance than the NMCFO nanoparticles, as evidenced by the drastically reduced diameter of these semicircle at high-frequency region in the electrochemical impedance spectroscopy (EIS) patterns (Fig. S10). As a result of lower contact and charge-transfer impedances, lithium ion diffusion and electron transfer are facilitated to give the greatly enhanced electrochemical performance of the NMCFO/OCNT composites. These results indicate that NMCFO/OCNT exhibits high electrochemical reversibility. The introduced OCNT can highly disperse NMCFO nanoparticles, prevent their aggregation, buffer the volume change, and promote effcient Li^+ diffusion and electronic

conduction, leading to better cycling stability and high rate performances.[48, 49] It should be pointed out that this preparation method is extendable to the preparation of other ferrite-based metal oxide (such as $Zn_aNi_bMn_cCo_dFe_2O_4$, $0 \leq a, b, c, d \leq 1$, $a+b+c+d=1$[40])/OCNT hybrid, and these materials can also be used as catalysis[50, 51] and supercapacitor, etc.[52]

4. Conclusions

In summary, we have prepared $Ni_{0.33}Mn_{0.33}Co_{0.33}Fe_2O_4$ (NMCFO) nanoparticles strongly coupled with oxidized carbon nanotubes (OCNT) network as anodes for Li-ion batteries. OCNT provides functional groups on the outer walls to nucleate and anchor NMCFO nanoparticles, leading to the hydrothermal formation of the NMCFO/OCNT composites. This unique hybrid structure remains a very stable capacity of 624.8 mAh g^{-1} after 200 cycles at a current density of 50 mA g^{-1}, and a high-rate capability at high current densities of 200–1000 mA g^{-1}. The super electrochemical properties of the NMCFO/OCNT composites should originate from the formed network structure with the intimate interconnection between NMCFO nanoparticles and OCNT, which not only provides stable electrical and ionic transfer channels, but also significantly shortens the diffusion length of the lithium ions. This work opens a new way for fabrication of ferrite-based metal oxide/OCNT nanocomposites as anode materials for Li-ion batteries.

Acknowledgments

The authors gratefully acknowledge the supports from the National Natural Science Foundation of China (No. 51272252) and Hundred Talents Program of the Chinese Academy of Sciences.

References

1 P. Poizot, S. Laruelle, S. Grugeon, L. Dupont and J. M. Tarascon, *Nature*, 2000, **407**, 496-499.

2 L. Zhang, H. B. Wu, S. Madhavi, H. H. Hng and X. W. Lou, *J. Am. Chem. Soc.*, 2012, **134**, 17388-17391.

3 J. Y. Wang, N. L. Yang, H. J. Tang, Z. H. Dong, Q. Jin, M. Yang, D. Kisailus, H. J. Zhao, Z. Y. Tang and D. Wang, *Angew. Chem. Int. Ed.*, 2013, **52**, 6417-6420.

4 K. T. Nam, D. W. Kim, P. J. Yoo, C. Y. Chiang, N. Meethong, P. T. Hammond, Y. M. Chiang and A. M. Belcher, *Science*, 2006, **312**, 885-888.

5 G. Q. Zhang, L. Yu, H. B. Wu, H. E. Hoster and X. W. Lou, *Adv. Mater.*, 2012, **24**, 4609-4613.

6 L. Zhou, D. Y. Zhao and X. W. Lou, *Adv. Mater.*, 2012, **24**, 745-748.

7 Z. Zhang, Y. Wang, Q. Tan, Z. Zhong and F. Su, *J. Colloid. Interf. Sci.*, 2013, **398**, 185-192.

8 B. Wang, H. B. Wu, L. Zhang and X. W. Lou, *Angew. Chem. Int. Ed.*, 2013, **52**, 4165-4168.

9 Z. Zhang, H. Chen, H. Che, Y. Wang and F. Su, *Mater. Chem. Phys.*, 2013, **138**, 593-600.

10 M. V. Reddy, T. Yu, C. H. Sow, Z. X. Shen, C. T. Lim, G. V. S. Rao and B. V. R. Chowdari, *Adv. Funct. Mater.*, 2007, **17**, 2792-2799.

11 H. Liu, X. W. Du, X. R. Xing, G. X. Wang and S. Z. Qiao, *Chem. Commun.*, 2012, **48**, 865-867.

12 Z. Y. Wang, D. Y. Luan, S. Madhavi, Y. Hu and X. W. Lou, *Energy Environ. Sci.*, 2012, **5**, 5252-5256.

13 H. D. Oh, S. W. Lee, S. O. Kim and J. K. Lee, *J. Power Sources*, 2013, **244**, 575-580.

14 M. Latorre-Sanchez, A. Primo and H. Garcia, *J. Mater. Chem.*, 2012, **22**, 21373-21375.

15 L. H. Zhuo, Y. Q. Wu, J. Ming, L. Y. Wang, Y. C. Yu, X. B. Zhang and F. Y. Zhao, *J. Mater. Chem. A*, 2013, **1**, 1141-1147.

16 M. Y. Cheng and B. J. Hwang, *J. Power Sources*, 2010, **195**, 4977-4983.

17 X. Huang, R. Wang, D. Xu, Z. Wang, H. Wang, J. Xu, Z. Wu, Q. Liu, Y. Zhang and X. Zhang, *Adv. Funct. Mater.*, 2013, **23**, 4345-4353.

18 G. Zhang, H. Wu, H. Hoster and X. W. Lou, *Energy Environ. Sci.*, 2014, **7**, 302-305.

19 Z. Zhang, Y. Wang, D. Li, Q. Tan, Y. Chen, Z. Zhong and F. Su, *Ind. Eng. Chem. Res.*, 2013, **52**, 14906-14912.

20 H. X. Zhang, C. Feng, Y. C. Zhai, K. L. Jiang, Q. Q. Li and S. S. Fan, *Adv. Mater.*, 2009, **21**, 2299-2304.

21 A. L. M. Reddy, M. M. Shaijumon, S. R. Gowda and P. M. Ajayan, *Nano Lett.*, 2009, **9**, 1002-1006.

22 P. R. Bueno and E. R. Leite, *J. Phys. Chem. B*, 2003, **107**, 8868-8877.

23 W. H. Shi, X. H. Rui, J. X. Zhu and Q. Y. Yan, *J. Phys. Chem. C*, 2012, **116**, 26685-26693.

24 L. Zhang, H. B. Wu and X. W. Lou, *Adv. Energy Mater.*, 2013, **4**, 1300958.

25 S. L. Candelaria, Y. Y. Shao, W. Zhou, X. L. Li, J. Xiao, J. G. Zhang, Y. Wang, J. Liu, J. H. Li and G. Z. Cao, *Nano Energy*, 2012, **1**, 195-220.

26 J. M. Tarascon and M. Armand, *Nature*, 2001, **414**, 359-367.

27 S. W. Lee, N. Yabuuchi, B. M. Gallant, S. Chen, B. S. Kim, P. T. Hammond and Y. Shao-Horn, *Nat. Nanotechnol.*, 2010, **5**, 531-537.

28 Z. Y. Cao and B. Q. Wei, *Energy Environ. Sci.*, 2013, **6**, 3183-3201.

29 Q. Zhang, J. Q. Huang, W. Z. Qian, Y. Y. Zhang and F. Wei, *Small*, 2013, **9**, 1237-1265.

30 J. H. Kim, K. H. Lee, L. J. Overzet and G. S. Lee, *Nano Lett.*, 2011, **11**, 2611-2617.

31 H. Zhang, G. P. Cao, Z. Y. Wang, Y. S. Yang, Z. J. Shi and Z. N. Gu, *Nano Lett.*, 2008, **8**, 2664-2668.

32 H. Li, J. K. Jo, L. Zhang, C. S. Ha, H. Suh and I. Kim, *Adv. Funct. Mater.*, 2010, **20**, 3864-3873.

33 D. Eder, *Chem. Rev.*, 2010, **110**, 1348-1385.

34 F. T. Edelmann, *Angew. Chem. Int. Ed.*, 1999, **38**, 1381-1387.

35 J. Liu, A. G. Rinzler, H. J. Dai, J. H. Hafner, R. K. Bradley, P. J. Boul, A. Lu, T. Iverson, K. Shelimov, C. B. Huffman, F. Rodriguez-Macias, Y. S. Shon, T. R. Lee, D. T. Colbert and R. E. Smalley, *Science*, 1998, **280**, 1253-1256.

36 M. A. Correa-Duarte, J. Perez-Juste, A. Sanchez-Iglesias, M. Giersig and L. M. Liz-Marzan, *Angew. Chem. Int. Ed.*, 2005, **44**, 4375-4378.

37 C. H. Xu, J. Sun and L. A. Gao, *J. Power Sources*, 2011, **196**, 5138-5142.

38 Y. Y. Liang, H. L. Wang, P. Diao, W. Chang, G. S. Hong, Y. G. Li, M. Gong, L. M. Xie, J. G. Zhou, J. Wang, T. Z. Regier, F. Wei and H. J. Dai, *J. Am. Chem. Soc.*, 2012, **134**, 15849-15857.

39 Z. Zhang, Y. Wang, M. Zhang, Q. Tan, X. Lv, Z. Zhong and F. Su, *J. Mater. Chem. A.*, 2013, **1**, 7444-7450.

40 Z. Zhang, Q. Tan, Y. Chen, J. Yang and F. Su, *J. Mater. Chem. A*, 2014, **2**, 5041-5050.

41 E. C. Alyea and M. A. Keane, *J. Catal.*, 1996, **164**, 28-35.

42 A. Demortiere, P. Panissod, B. P. Pichon, G. Pourroy, D. Guillon, B. Donnio and S. Begin-Colin, *Nanoscale*, 2011, **3**, 225-232.

43 V. Georgakilas, D. Gournis, V. Tzitzios, L. Pasquato, D. M. Guldi and M. Prato, *J. Mater. Chem.*, 2007, **17**, 2679-2694.

44 C. Vidal-Abarca, P. Lavela and J. L. Tirado, *Solid State Ionics*, 2010, **181**, 616-622.

45 J. Y. Yao, P. Xiao, Y. H. Zhang, M. Zhan, F. Yang and X. Q. Meng, *J. Alloy. Compd.*, 2014, **583**, 366-371.

46 Y. Z. Su, S. Li, D. Q. Wu, F. Zhang, H. W. Liang, P. F. Gao, C. Cheng and X. L. Feng, *ACS Nano*, 2012, **6**, 8349-8356.

47 A. Latz and J. Zausch, *J. Power Sources*, 2011, **196**, 3296-3302.

48 X. H. Wang, X. W. Li, X. L. Sun, F. Li, Q. M. Liu, Q. Wang and D. Y. He, *J. Mater. Chem.*, 2011, **21**, 3571-3573.

49 L. Q. Tao, J. T. Zai, K. X. Wang, H. J. Zhang, M. Xu, J. Shen, Y. Z. Su and X. F. Qian, *J. Power Sources*, 2012, **202**, 230-235.

50 P. Lee, H. Teng and C. Yeh, *Nanoscale*, 2013, **5**, 7558-7563.

51 S. Chen and S. Z. Qiao, *ACS Nano*, 2013, **7**, 10190-10196.

52 Z. Yu, L. Chen and S. Yu, *J. Mater. Chem. A*, 2014, DOI: 10.1039/c1034ta00492b.

List of Table

Figure Captions:

Table 1. The electrochemical performance of all the samples.

Samples	$C_{1st\text{-}di}$ [a] (mAh g^{-1})	$C_{1st\text{-}ch}$ [b] (mAh g^{-1})	CE_{in} [c] (%)	ACE_{2nd} [d] (%)	ACF_{100th} [e] (%/cycle)	C_{100th} [f] (mAh g^{-1})
NMCFO	1541.3	723.2	46.9	94.5	0.804	141.8
NMCFO/OCNT-1	1092.1	692.2	63.4	97.4	0.028	673.7
NMCFO/OCNT-2	1252.2	771.5	61.6	97.2	0.050	733.1
NMCFO/OCNT-3	1452.2	909.1	62.7	97.0	0.219	710.3
NMCFO/OCNT-4	1495.1	928.5	62.1	96.8	0.455	506.3

a: $C_{1st\text{-}di}$, the first discharge capacity;

b: $C_{1st\text{-}ch}$, the first charge capacity;

c: CE_{in}, the initial coulombic efficiency;

d: ACE_{2nd}, the average coulombic efficiency after second cycles;

e: ACF_{100th}, average capacity fading rate during 100 cycles;

f: C_{100th}, the discharge capacity after 100 cycles.

List of Figures:

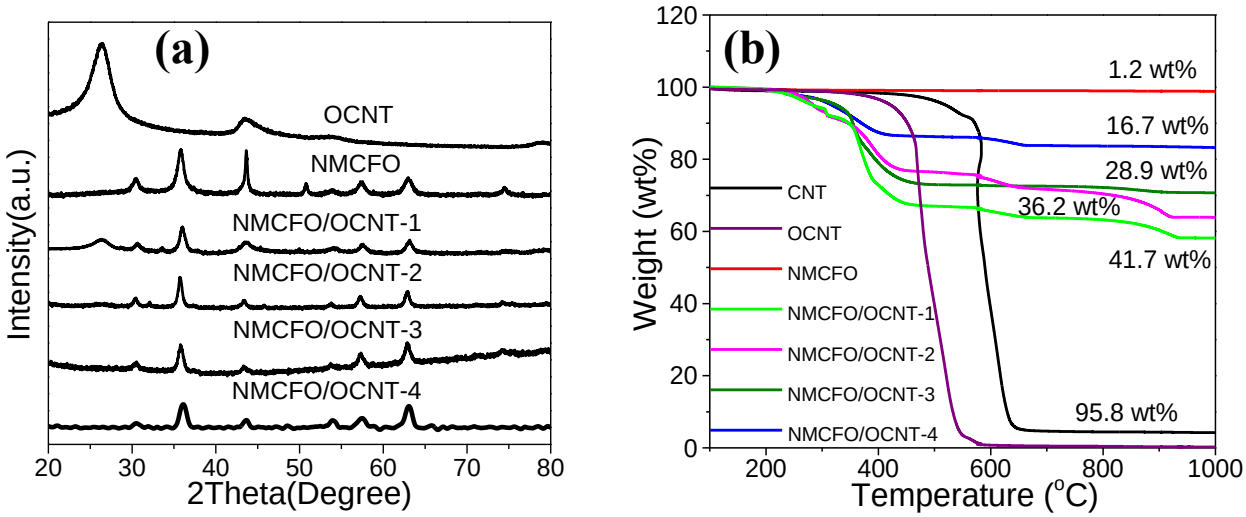

Fig. 1

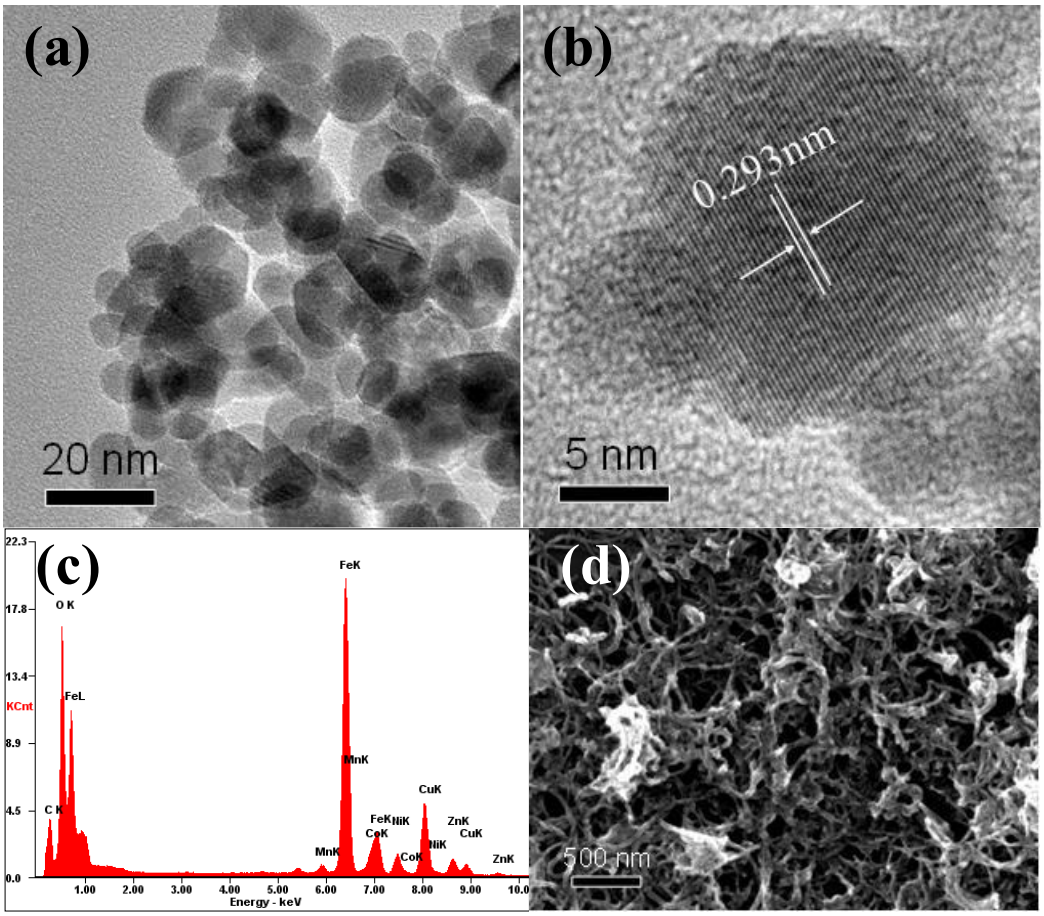

Fig. 2

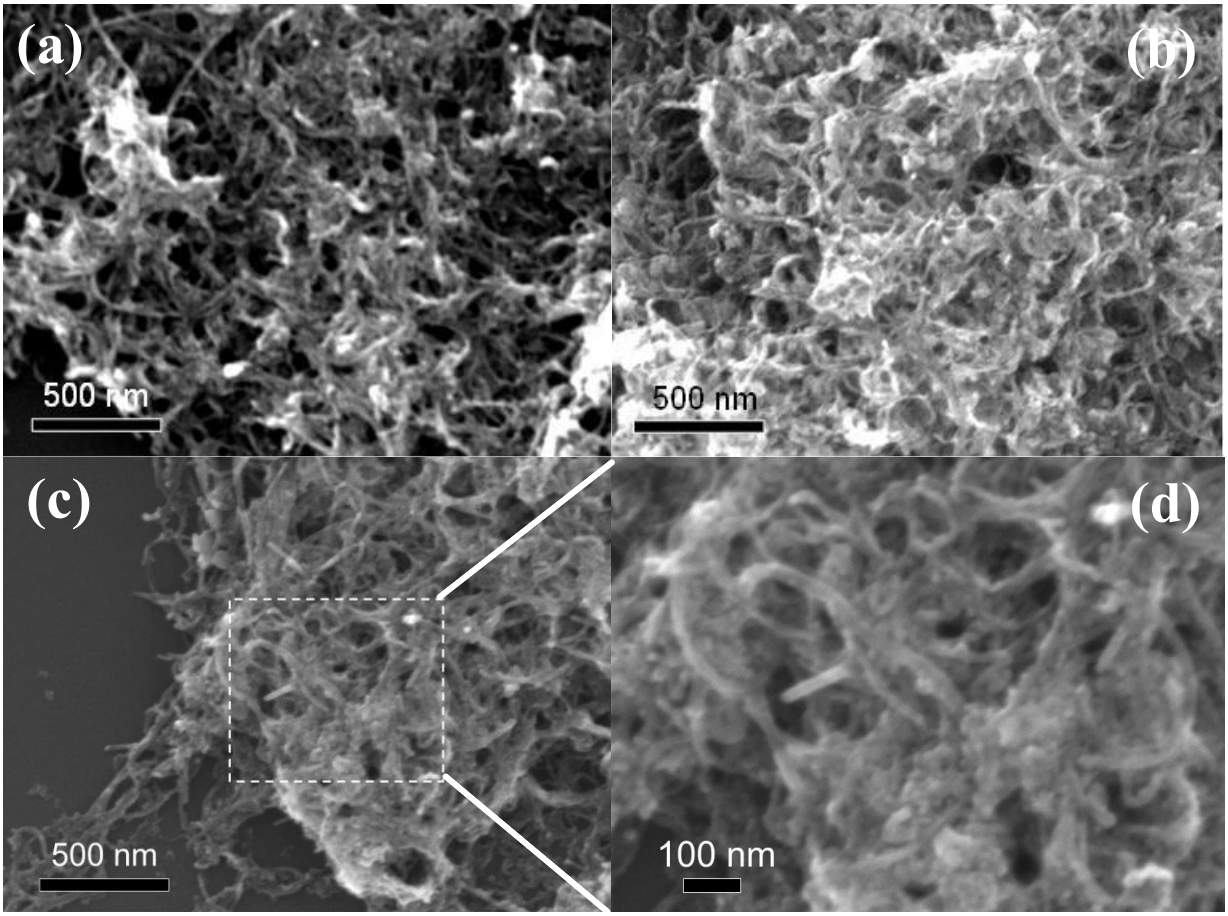

Fig. 3

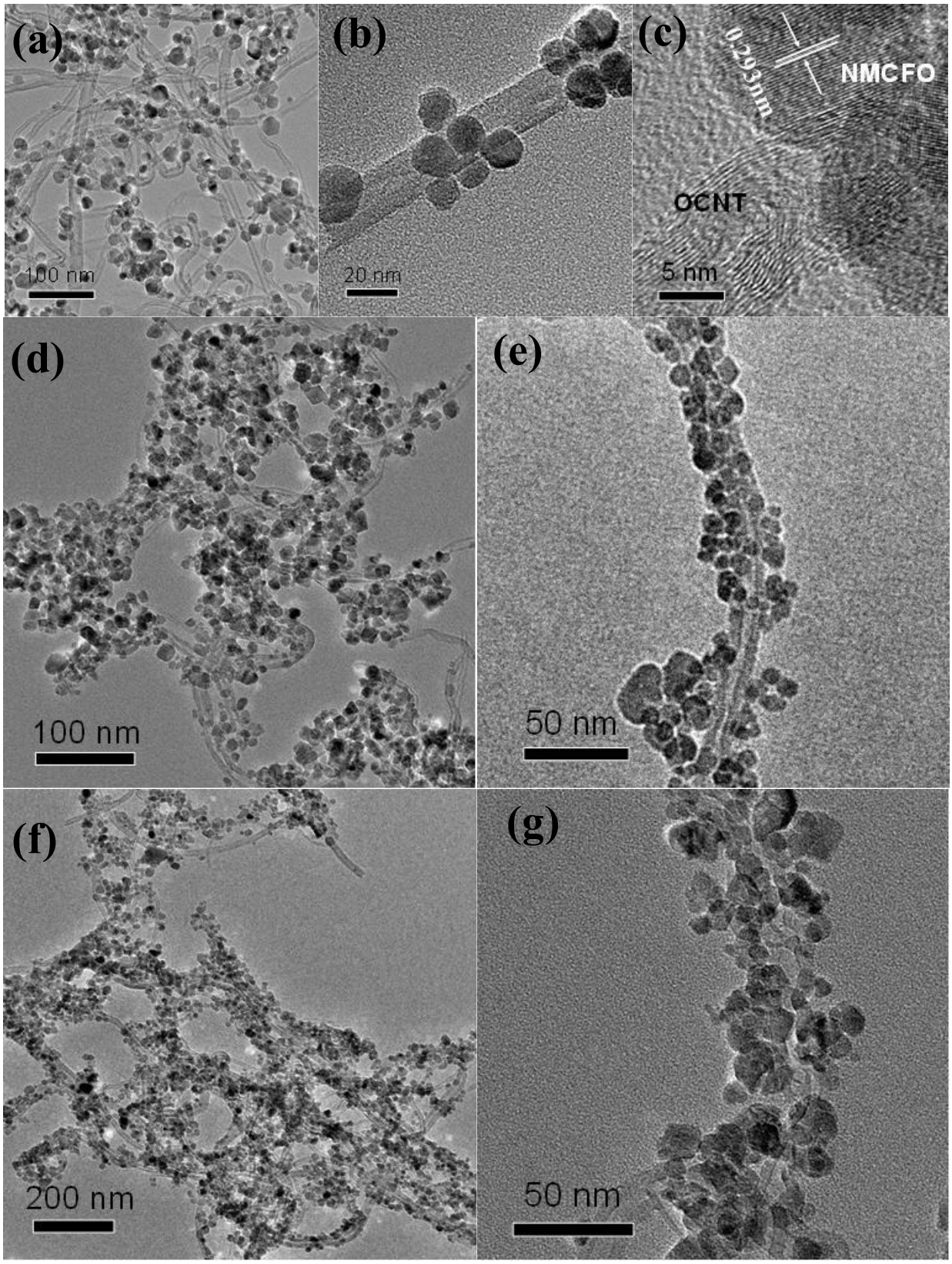

Fig. 4

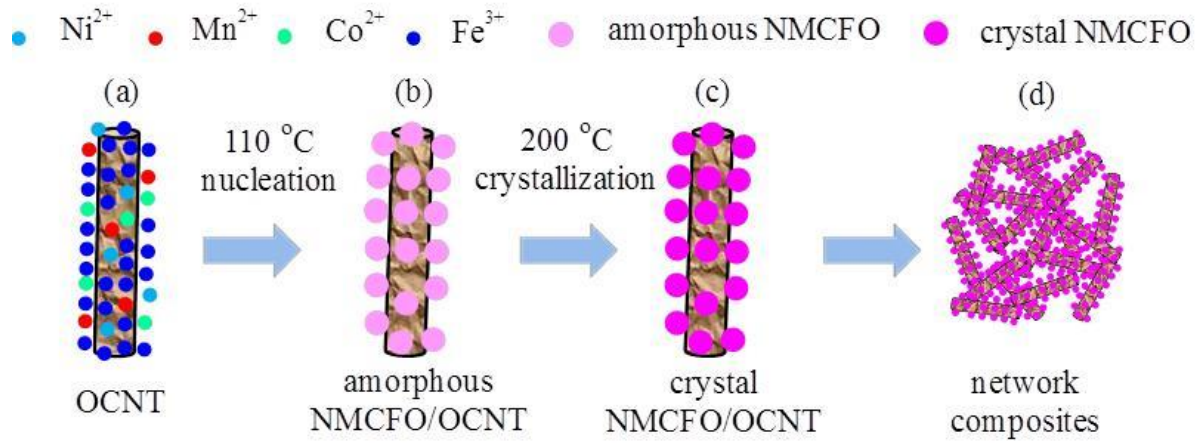

Fig. 5

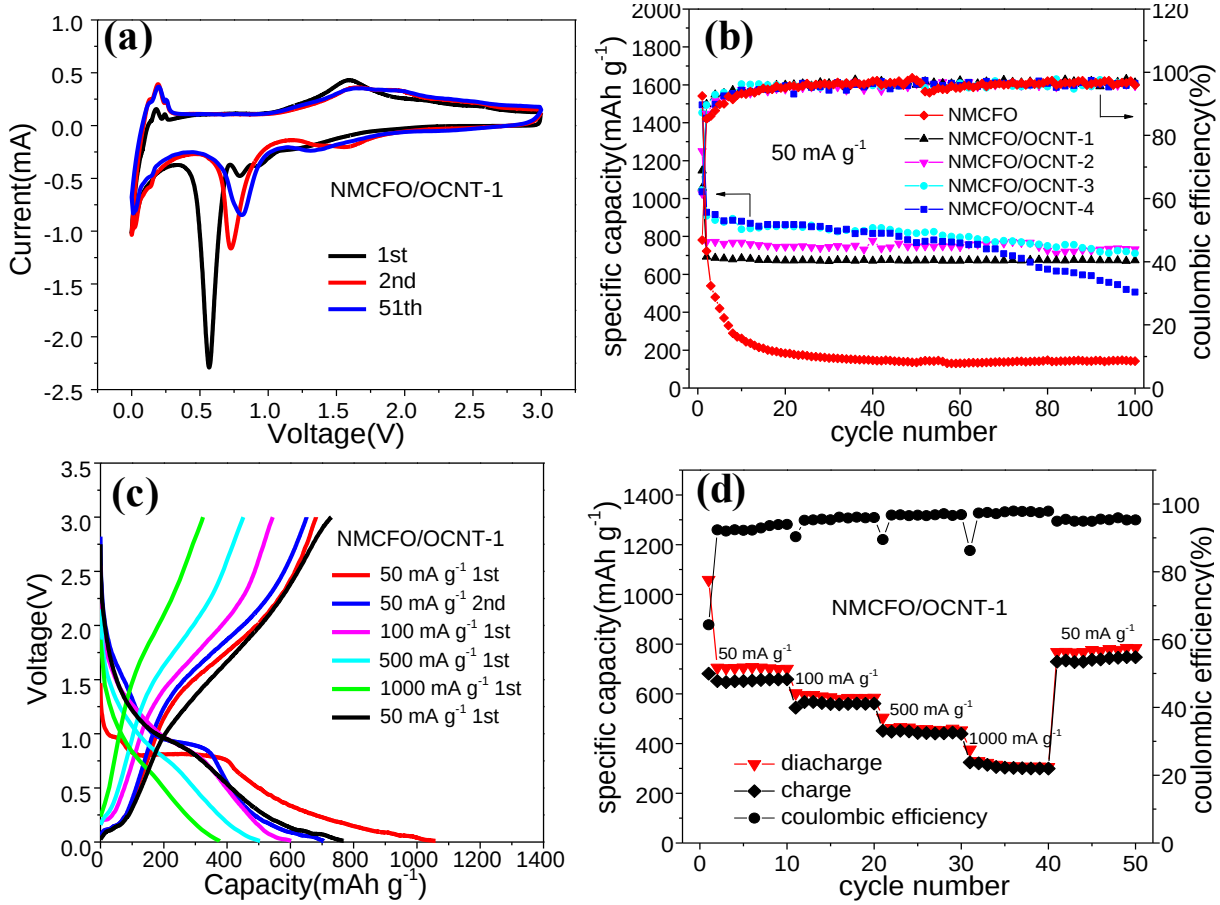

Fig. 6